Structural phase transitions and electronic phenomena at 180-degree domain walls in rhombohedral $BaTiO_3$

Eugene A. Eliseev,[1] Peter V. Yudin,[2] Sergei V. Kalinin,[3] Nava Setter,[2] Alexander K. Tagantsev,[2] and Anna N. Morozovska[4,*]

[1]*Institute for Problems of Materials Science, National Academy of Sciences of Ukraine, 3, Krjijanovskogo, 03142 Kiev, Ukraine*

[2]*Ceramics Laboratory, Swiss Federal Institute of Technology (EPFL), CH-1015 Lausanne, Switzerland*

[3]*Center for Nanophase Materials Science, Oak Ridge National Laboratory, Oak Ridge, Tennessee, 37831, USA*

[4]*Institute of Physics, National Academy of Sciences of Ukraine, 46, pr. Nauki, 03028 Kiev, Ukraine*

(Received 29 September 2012; published 25 February 2013)

The structure and electronic phenomena at the 180-degree domain wall in the rhombohedral phase of $BaTiO_3$ are described using Landau-Ginzburg-Devonshire theory. Dependent on the wall orientation, two types of domain wall behaviors are identified. The low-energy "achiral" phase occurs in the vicinity of the {110} orientation and has odd polarization profile invariant with respect to inversion about the wall center. The "chiral" phase occurs around {211} wall orientations and corresponds to mixed parity domain walls. The temperature-induced transformation between the phases is abrupt and is accompanied with 20%–30% change of the domain wall thickness. This process gives rise to the significant changes of the electronic structure of the wall. Depending on the temperature and flexoelectric coupling strength, relative conductivity of the wall becomes at least one order of magnitude higher than in the single-domain region. The possible strategies for exploring these transitions based on direct measurements of domain wall width and conductive atomic force microscopy are discussed.

DOI: 10.1103/PhysRevB.87.054111 PACS number(s): 77.80.Dj, 77.22.Ej

I. INTRODUCTION

Structure and properties of ferroelectric domain walls (DWs) have been remaining the objects of endless fascination by the condensed matter physics community since the early days of ferroelectricity. In particular, the structure of DWs has been explored both experimentally[1,2] and theoretically[3–6] for several decades, with recent impetus derived from advances in electron microscopy and scanning probe microscopy techniques that allowed atomic-level probing of order parameter fields and electronic wall functionality.[7–10] This in turn has stimulated extensive effort in theoretical understanding of structure and order parameter couplings at the domain walls. To date, most theoretical studies have been performed using the continuum Landau-Ginzburg-Devonshire (LGD) theory.[3–6,11–14] Despite the fact that intrinsic width of DWs in ferroelectrics is of the order of several lattice constants, domain wall structure calculated using LGD has been found in good agreement with that derived from density functional theory (DFT).[15–17] These studies have further elucidated a broad spectrum of novel phenomena at the walls, including emergence of secondary order parameters, magnetic and structural order phase transitions,[18–20] and multiple electronic phenomena.

One of the interesting features of ferroelectric DW forecasted theoretically, but not yet observed experimentally, is the transition between one-component and two-component polarization profiles, i.e., intrinsic symmetry-breaking transition in the wall planes. For a general Ising model, such transition was predicted long ago by Lajzerowicz and Niez[21] in 1979. LGD theory of the phenomenon in a real ferroelectric material was developed only recently by Hlinka *et al*. for the rhombohedral phase of $BaTiO_3$ (BTO).[6,14,17] For this system, Bloch walls with a large rotating component have been predicted.[6] While for the {211} orientations, the wall structure has been shown to undergo the symmetry breaking transition[14] to chiral phase. However, the scope of the studies[6,14,17] have been restricted to several special wall orientations, so that the questions about energetically preferable orientations and guidelines for the experimental observation of the phase transition in the walls still remain open. Furthermore, unexplored was the impact of the flexoelectricity, i.e., the bilinear coupling of polarization with a strain gradient,[22,23] while the flexoelectricity-related electromechanical effects are known to be important for the physics of nanosized ferroelectric with polarization gradient.[24–29]

Note that the concept of Bloch and Neel-type domain walls was introduced by Lee *et al*.[30] These considerations motivate us to perform LGD-based study of 180-degree DW structure in the rhombohedral phase of BTO, exploring the angular anisotropy of DW energy and specifically addressing the role of flexoelectric coupling. These studies predict the existence of phase transitions between chiral and *achiral* wall structures induced by temperature or wall rotation, and suggest the presence of additional one-dimensional (1D) topological defects within the walls. We further explore the electronic phenomena at these walls related to the presence of the polarization component perpendicular to the wall plane. Resultant free charges accumulation is predicted to be sufficiently large to be detected by conductive AFM (c-AFM), suggesting possible experimental strategy for exploring this behavior.

The structure of the article is as follows. In Sec. II we describe the properties of the 180-degree domain walls within GLD phenomenology. The effect of the flexoelectric coupling on the wall structure is considered in Sec. III. Finally, the electronic phenomena and conductivity changes at the domain walls are discussed in Sec. IV.

II. STRUCTURE OF THE 180-DEGREE DOMAIN WALL

Here we analyze the structure of the 180-degree domain wall within the framework of simple LGD theory neglecting

flexoelectric coupling and semiconducting properties of BTO (dielectric limit). The validity of the dielectric approximations is analyzed in this section, illustrating that the conductivity has negligible influence on DW structure and intrinsic energy.

A. Statement of the problem

We consider nominally uncharged 180-degree DW in the bulk of BTO single crystal. According to recent LGD and DFT studies Ising-Bloch type[14,17] and mixed Ising-Bloch-Néel type[30,31] 180-degree walls can exist in a wide class of ferroelectric materials, including BTO. Thus, a polarization vector inside a DW in BTO can have all three components. The component P_3, parallel to the spontaneous polarization $\pm P_S$ in the domains, is regarded as the Ising type; the component P_2, parallel to the wall plane, but perpendicular to the Ising-type component, which vanishes far from the wall, is regarded as the Bloch-type component; and component P_1, normal to the wall, is regarded as the Néel-type component [see Fig. 1(a)]. Note that the Néel-type component P_1 is associated with the nonzero divergence of the polarization vector and hence should be considered jointly with associated depolarization fields.

We analyze the polarization profile in the DW region within LGD theory. We introduce Gibbs potential G with $dG = E_i dP_i - u_{ij} d\sigma_{ij}$, where E_i is the electric field (including the depolarization field), u_{ij} are elastic strains, σ_{ij} are elastic stresses, and P_i are polarization components related to the soft mode. For the $m\bar{3}m$ symmetry in the crystallographic frame the expression for the Gibbs potential has the form (see, e.g., Refs. 32–34)

$$G = G_{\text{polar}} + G_{\text{grad}} + G_{\text{striction}} + G_{\text{elastic}}, \tag{1}$$

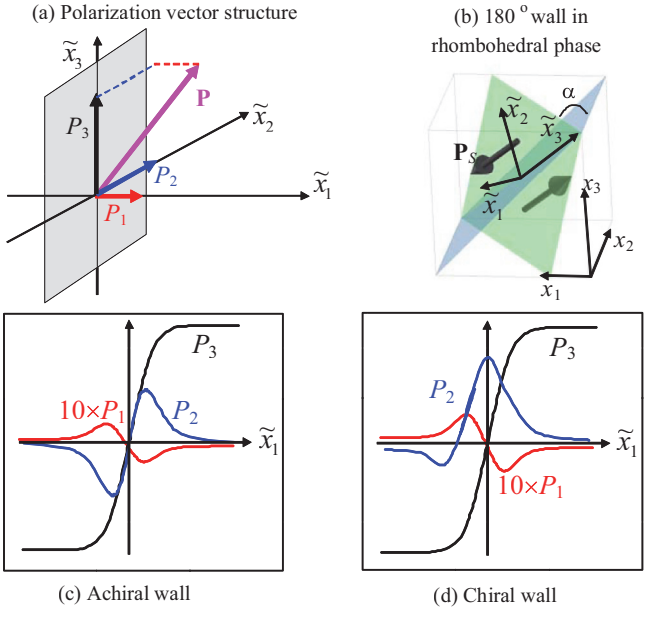

FIG. 1. (Color online) (a) Polarization vector structure. (b) Rotated coordinate frame $\{\tilde{x}_1,\tilde{x}_2,\tilde{x}_3\}$ choice for 180-degree nominally uncharged domain walls in the rhombohedral ferroelectric BTO; α is the wall rotation angle counted from crystallographic plane $\langle 101\rangle$. The distance from the wall plane is $\tilde{x}_1$. (c) and (d) Schematics of the polarization components distribution inside achiral and chiral domain walls.

where $G_{\text{polar}} = a_i P_i^2 + a_{ij} P_i^2 P_j^2 + a_{ijk} P_i^2 P_j^2 P_k^2$ is the Landau part, $G_{\text{grad}} = \frac{g_{ijkl}}{2} \frac{\partial P_i}{\partial x_j} \frac{\partial P_k}{\partial x_l}$ is the gradient or Ginsburg part, $G_{\text{striction}} = -Q_{ijkl}\sigma_{ij} P_k P_l$ is the electrostriction term, and $G_{\text{elastic}} = -\frac{s_{ijkl}}{2}\sigma_{ij}\sigma_{kl}$ is the elastic contribution. Hereinafter a_i, a_{ij}, and a_{ijk} are the LGD-expansion coefficients of the second, fourth, and sixth order dielectric stiffness tensors correspondingly, gradient coefficients are g_{ijkl}, Q_{ijkl} are fourth second rank electrostriction tensors coefficients, and s_{ijkl} are elastic compliances. Numerical values of the tensor components are collected from Refs. 6 and 34–37 and listed in Table S1 of the Supplemental Material.[38]

Since all physical quantities can depend only on the distance $\tilde{x}_1$ from the DW plane $\tilde{x}_1 = 0$, we introduce the coordinate system $\{\tilde{x}_1,\tilde{x}_2,\tilde{x}_3\}$ rotated with respect to the cubic crystallographic axes $\{x_1,x_2,x_3\}$ as shown in Fig. 1(b). Here α is the wall rotation angle around the cube spatial diagonal with respect to the $\langle 101\rangle$ plane. Equation (1) can then be rewritten in the coordinate system $\{\tilde{x}_1,\tilde{x}_2,\tilde{x}_3\}$ to obtain $\tilde{G}$ and to derive the Euler-Lagrange equations[39] for polarization components $\tilde{P}_i$ and equations of state for elastic stresses $\tilde{\sigma}_{ij}$ correspondingly:

$$\frac{\partial \tilde{G}}{\partial \tilde{P}_i} - \frac{\partial(\partial \tilde{G})}{\partial(\partial \tilde{P}_i/\partial \tilde{x}_1)} = \tilde{E}_i, \tag{2a}$$

$$\frac{\partial \tilde{G}}{\partial \tilde{\sigma}_{ij}} = -\tilde{u}_{ij}. \tag{2b}$$

The external field is regarded absent, so $\tilde{E}_2 = \tilde{E}_3 = 0$. The depolarization field $\tilde{E}_1^d$, caused by the inhomogeneity of $\tilde{P}_1(\tilde{x}_1)$, can be derived from the Maxwell equation div$\mathbf{D} = 0$, where $\mathbf{D}$ is the electric displacement as[12]

$$\tilde{E}_1^d(\tilde{x}_1) \approx \frac{-\tilde{P}_1(\tilde{x}_1)}{\varepsilon_0 \varepsilon_b}. \tag{3}$$

Here $\varepsilon_0 = 8.85 \times 10^{-12}$ F/m is the universal dielectric constant and ε_b is the background dielectric permittivity unrelated with the soft mode.[40] The boundary conditions are $\tilde{P}_3(\tilde{x}_1 \to \pm\infty) = \pm\tilde{P}_S$, $\tilde{P}_{1,2}(\tilde{x}_1 \to \pm\infty) \to 0$, $\tilde{E}_1(\tilde{x}_1 \to \pm\infty) \to 0$, and $\tilde{\sigma}_{ij}(\tilde{x}_1 \to \pm\infty) = 0$.

Mechanical variables can be eliminated by solving equations of state along with the mechanical equilibrium conditions $\partial \tilde{\sigma}_{1j}/\partial \tilde{x}_1 = 0$ and compatibility relation $e_{i1l} e_{j1n} (\partial^2 \tilde{u}_{ln}/\partial \tilde{x}_1^2) = 0$. Explicit form of these equations and elastic stresses in the rotated coordinate frame are listed in Appendixes S1 and S2.[38] Below we present the results of numerical calculations based on Eqs. (2) and (3).

B. DW structure

The analysis of the polarization profiles yields two classes of solutions, corresponding to chiral and achiral wall structures. The wall is achiral if its profile is invariant upon the inversion with respect to the wall center. In the achiral wall all the components are odd functions of the $\tilde{x}_1$ coordinate [Fig. 1(c)]. In the chiral wall type the components $\tilde{P}_1(\tilde{x}_1)$ and $\tilde{P}_2(\tilde{x}_1)$ are of mixed $\tilde{x}_1$ parity, i.e., contain odd and even components [Fig. 1(d)]. As follows from the symmetry of the problem (the governing equations and boundary conditions are invariant upon the inversion with respect to the wall center), the chiral walls are bistable, corresponding to additional symmetry

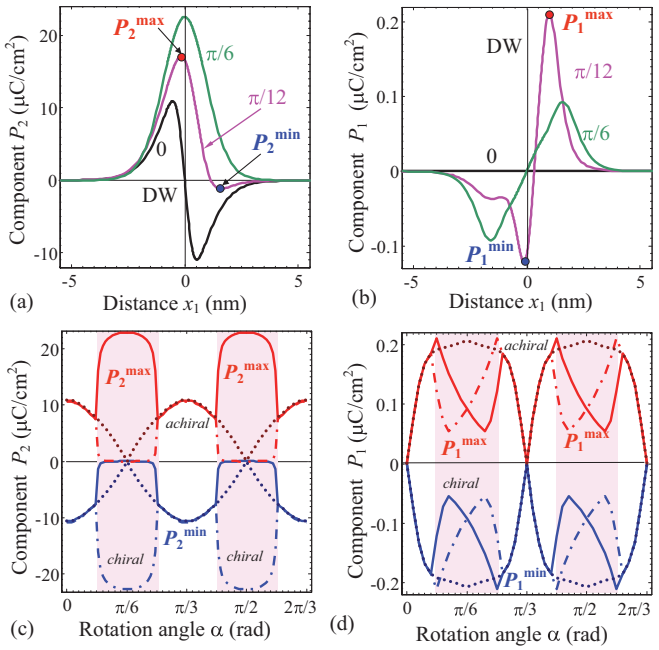

FIG. 2. (Color online) Profiles of polarization components (a) $\tilde{P}_2(\tilde{x}_1)$ and (b) $\tilde{P}_1(\tilde{x}_1)$ calculated across the DW for rotation angles $\alpha = 0, \pi/12, \pi/6$ (specified near the curves), temperature 180 K, and BTO parameters listed in Table S1.[38] Angular dependence of maximal (red upper curves labeled $\tilde{P}_i^{max}$) and minimal (blue bottom curves labeled $\tilde{P}_i^{min}$) values of (c) $\tilde{P}_2(\tilde{x}_1)$ and (d) $\tilde{P}_1(\tilde{x}_1)$. Absolutely stable solutions are shown by the solid and dash-dotted curves for left- and right-handed solutions correspondingly. Achiral solutions are shown by dotted curves. Filled rectangles indicate the region of absolute stability of chiral walls. Empty regions correspond to achiral wall absolute stability regions.

breaking in the wall plane. In both wall types all three components of polarization are present. Note that in contrast to the tetragonal symmetry,[41] in the rhombohedral phase the component $\tilde{P}_1(\tilde{x}_1)$ is nonzero even under the absence of the flexoelectric coupling.

Distributions of polarization components $\tilde{P}_1(\tilde{x}_1)$ and $\tilde{P}_2(\tilde{x}_1)$ across the 180-degree wall are shown in Figs. 2(a) and 2(b) for $\alpha = 0, \pi/12, \pi/6$ correspondingly. The Ising component $\tilde{P}_3(\tilde{x}_1)$ (not shown) has a standard kink profile, which is weakly α dependent. Interestingly, $\tilde{P}_1(\tilde{x}_1)$ is about two order of magnitude smaller than $\tilde{P}_2(\tilde{x}_1)$ as it is suppressed by the depolarizing field $\tilde{E}_1(\tilde{x}_1)$. The screening phenomena at the wall and associated changes in the conductivity are analyzed in Sec. IV.

The numerical analysis of Eqs. (2) and (3) suggests that the structure of the wall is strongly dependent on the orientation. This behavior is illustrated in Figs. 2(c) and 2(d) by plotting maximal and minimal values of the components $\tilde{P}_i^{max}$ and $\tilde{P}_i^{min}$ as functions of the domain wall rotation angle α. The achiral solution [dotted line in Figs. 2(c) and 2(d)] exists for any DW orientation. However, for the wall orientations around $\alpha = \pi/6 + m\pi/3$ $(m = 0,1,2,\ldots)$ this solution becomes metastable, and the chiral solution becomes energetically preferable (see Fig. 3 from Sec. II C). The true solutions, corresponding to minimal intrinsic energy, are shown by the solid and dash-dotted curves for left- and

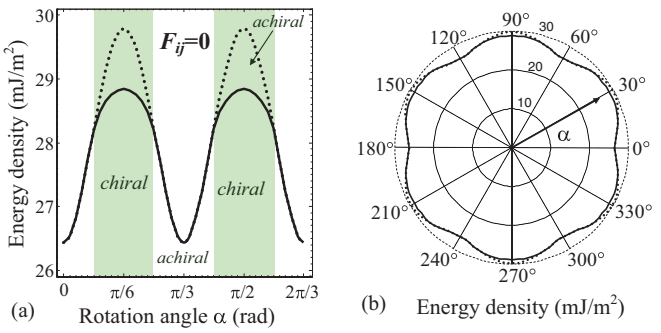

FIG. 3. (Color online) (a) Angular dependence and (b) polar plot of the 180-degree DW energy density calculated for BTO at 180 K. Solid curves correspond to the true solution. The energy of achiral solution is shown by dotted curves. Filled and empty rectangles indicate the regions of absolute stability of chiral and achiral solutions, respectively.

right-handed solutions, respectively, in Figs. 2(c) and 2(d). Thus if we virtually rotate the DW, it undergoes a phase transition from achiral to chiral state at $\alpha \approx (2m+1)\pi/12$, $m = 0,1,2$.

C. DW energy

To calculate the free energy of the DW we perform the Legendre transformation of the potential (1)[42] as $F = \int_{-\infty}^{\infty} (\tilde{G} + \tilde{u}_{ij}\tilde{\sigma}_{ij} - \tilde{P}_1\tilde{E}_1^d/2)d\tilde{x}_1$. Dependencies of the DW energy on the wall orientation are shown in Fig. 3. The obtained energy anisotropy [see polar plot Fig. 3(b)] explains the anisotropic hexagonlike domains observed experimentally in BTO.[43] One can see from Fig. 3(a) that energetically preferable orientations $\alpha = m\pi/3$, $m = 0,1,2$ correspond to achiral walls. In contrast, chiral walls are realized in the vicinity of the energy maximums $\alpha = \pi/6 + m\pi/3$.

D. Phase transition in the wall

The two possible wall structures suggest the existence of symmetry breaking transitions and associated topological defects within the walls (similar to cross-tie defects in ferromagnets). Note that chiral phase transitions inside DW were predicted by Lajzerowicz and Niez.[21] Using the three-dimensional Ising model they studied a domain wall state as a function of anisotropy (K) and temperature (T) and have shown that the wall undergoes a phase transition in the K, T plane, with the chirality as the order parameter. Hlinka *et al.*[14] suggested to apply mechanical stress to switch {211} DW between chiral and achiral phases in the rhombohedral BTO. Here we observe both chiral and achiral phases at zero stress, and proceed to explore the temperature- and orientation-driven phase transition possible between the two phases. Note that while thermal transitions are trivial, the orientation-driven transition can be visualized, virtually rotating the domain wall from the achiral {110} "ground state" to the chiral state. Experimentally this can be explored by rotational anisotropy of properties along the wall of a cylindrical domain wall where the phase transition occurs in certain spatial points.

To explore this behavior systematically and analyze angular and temperature dependence of chirality, we introduce relevant

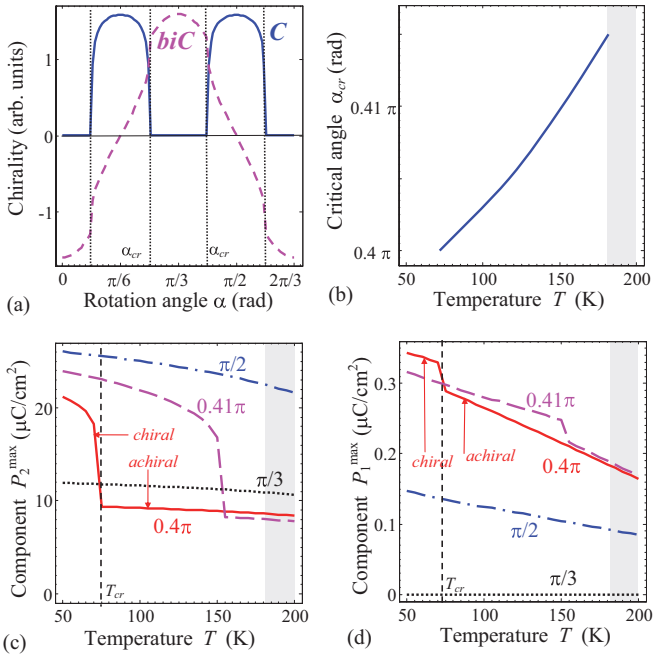

FIG. 4. (Color online) (a) Chirality C (solid curve) and bichirality biC (dashed curve) vs wall rotation angle α calculated for BTO at 180 K. Only the left-handed wall is shown. (b) Temperature dependence of the maximal values of (c) $\tilde{P}_2$ and (d) $\tilde{P}_1$ calculated for different rotation angles $\alpha = \pi/3$ (minimal energy); $\alpha = \pi/2$ (maximal energy), and $\alpha = 0.4\pi, 0.41\pi$ (phase transition) specified near the curves. Gray rectangles in plots (b)–(d) indicate the region of orthorhombic and rhombohedral phases coexistence.[63]

order parameters. As a measure of chirality we utilize the parameter

$$C = \int_{-\infty}^{\infty} \left(\tilde{P}_3 \frac{d\tilde{P}_2}{d\tilde{x}_1} - \tilde{P}_2 \frac{d\tilde{P}_3}{d\tilde{x}_1} \right) d\tilde{x}_1$$

introduced by Salje *et al.*[44] In a similar manner we introduce the chiral dipole moment or "bichirality"

$$biC = \int_{-\infty}^{\infty} \left(\tilde{P}_3 \frac{d\tilde{P}_2}{d\tilde{x}_1} - \tilde{P}_2 \frac{d\tilde{P}_3}{d\tilde{x}_1} \right) \tilde{x}_1 d\tilde{x}_1.$$

The C and biC parameters characterize even and odd polarization component $\tilde{P}_2$, respectively.

The orientation-driven phase transition from achiral to chiral state is illustrated in Fig. 4. The transition happens at angles $\alpha_{\rm cr}^m \approx \pi/6 \pm \pi/12 + m\pi/3$ for $T \approx 170$–200 K. The critical angles exhibit some weak temperature dependence, as shown in Fig. 4(b), for the $\alpha_{\rm cr}^* \approx 5\pi/12$. Thus there is a narrow region of wall orientations $0.4\pi - 0.415\pi$, where phase transition may be achieved by temperature change at constant wall orientation, as illustrated in Fig. 4(b). The behavior of polarization components $\tilde{P}_2$ and $\tilde{P}_1$ near such temperature-driven phase transition is illustrated in Figs. 4(c) and 4(d), where a noticeable jump of their maximal values is observed. The jump of the component $\tilde{P}_2$ [Fig. 4(c)] is not small (about two times), and we dare to propose the way of its experimental observation through its correlation with the relatively small jump on the component $\tilde{P}_1$ [Fig. 4(d)], which can be detected from c-AFM at different temperatures, as it will

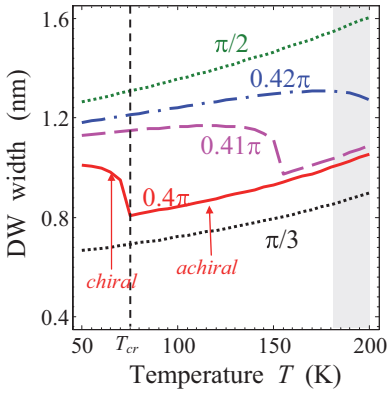

FIG. 5. (Color online) Temperature dependence of DW width calculated in rhombohedral phase of BTO for different rotation angles $\alpha = \pi/2, \pi/3, 0.4\pi, 0.41\pi, 0.42\pi$ specified near the curves. Gray rectangles indicate the region of orthorhombic and rhombohedral phases coexistence.

be discussed in Sec. IV. The big jump on the component $\tilde{P}_2$ can lead to the nontrivial behavior of the DW width in the vicinity of the phase space point $\{\alpha_{\rm cr}^*, T_{\rm cr}^*\}$, where the achiral wall becomes more stable than the chiral one. Figure 5 demonstrates such temperature behavior of the DW width calculated for the Ising polarization component $\tilde{P}_3$ at the level 0.5 with respect to the saturation value. Since the jump on DW width is of the order of 20% (see solid and dashed curves in Fig. 5), the predicted temperature-induced phase transition from chiral to achiral wall can potentially be verified experimentally from the domain wall width temperature measurements by using high-resolution electron microscopy.

III. IMPACT OF THE FLEXOELECTRIC COUPLING

We further explore the role of flexoelectric coupling on the wall structure. To take into account the flexoelectric contribution we add the term (see, e.g., Refs. 23,25,29,32, and 45)

$$G_f = \frac{\tilde{F}_{ijkl}}{2} \left(\tilde{\sigma}_{ij} \frac{\partial \tilde{P}_k}{\partial \tilde{x}_l} - \tilde{P}_k \frac{\partial \tilde{\sigma}_{ij}}{\partial \tilde{x}_l} \right) \qquad (4)$$

into the Gibbs potential (1), where $\tilde{F}_{ijkl}$ is the flexoelectric tensor. This leads to the inhomogeneity in Euler-Lagrange equations: $-\tilde{F}_{12}(\partial\tilde{\sigma}_2/\partial\tilde{x}_1) - \tilde{F}_{13}(\partial\tilde{\sigma}_3/\partial\tilde{x}_1) - 2\tilde{F}_{14}(\partial\tilde{\sigma}_4/\partial\tilde{x}_1)$ in equation for $\tilde{P}_1$, $2\tilde{F}_{15}\partial\tilde{\sigma}_4/\partial\tilde{x}_1$ in equation for $\tilde{P}_2$, and $\tilde{F}_{15}\partial\tilde{\sigma}_2/\partial\tilde{x}_1$ in equation for $\tilde{P}_3$ (see Appendix S3[38]).

The numerical analysis of resultant GLD energy suggests that the flexoelectric coupling introduces additional angular anisotropy for the DW structure and energy. As shown in Fig. 6(a), the modulation period of polarization component $\tilde{P}_1$ changes from $\pi/3$ without flexoelectric coupling to $2\pi/3$ for nonzero flexoelectric coupling, resulting in additional symmetry breaking between the states. Remarkably, the ground states at $\alpha = m\pi/3$ stay equivalent, while the energy maxima at $\alpha = \pi/6 + m\pi/3$ for odd and even m become nonequivalent [Fig. 6(b)]. This is seen from the different width of the area of chiral wall absolute stability and different height of the energy maximum. Note that the equivalence of the minima follows from the symmetry of the problem, which contains

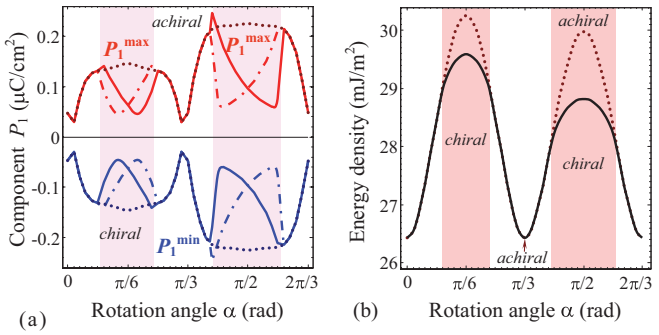

FIG. 6. (Color online) (a) Angular dependence of maximal (red upper curves labeled $\tilde{P}_1^{\max}$) and minimal (blue bottom curves labeled $\tilde{P}_1^{\min}$) values of polarization component $\tilde{P}_1$ in the 180-degree DW region calculated for BTO, temperature 180 K, flexoelectric coefficients $F_{11} = 2.46$, $F_{12} = 0.48$, $F_{44} = 0.05$ in 10^{-11} m^3/C were taken from *ab initio* calculations;[37,64] all designations are the same as in the Fig. 2(d). (b) Angular dependence of the DW energy density; all designations are the same as in the Fig. 3(a).

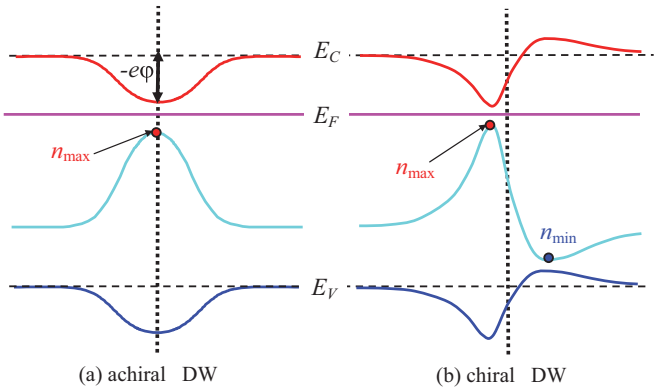

FIG. 7. (Color online) Sketches of local band bending for (a) achiral and (b) chiral walls, where the spatial regions with maximal ($n_{\max}$) and minimal ($n_{\min}$) electron density are indicated.

the axis of the third order along [111] and the mirror plane {110}. For the maxima the situation is different since there is no mirror plane at {211} and the only symmetry operation is the axis of the third order. Hence, the flexoelectric effect lifts the degeneracy of the maxima and reveals the true symmetry of the problem, which was not reflected in the approximation without the coupling (see Appendix S4[38]). Note that the flexoelectric contribution in the DW energy is comparable with energy anisotropy originated from electrostriction.

Polarization component $\tilde{P}_1$ appeared much more sensitive to the flexoelectric coupling than $\tilde{P}_2$ (see Table I). At the same time, the component $\tilde{P}_3$ appears almost insensitive to the coupling value. Due to the coupling, $\tilde{P}_1$ amplitude is nonzero for all rotation angles including $\alpha = m\pi/3$, while it is still minimal for this angle [compare Figs. 2(d) and 6(a)]. Thus flexoelectric coupling acts as an additional and relatively strong source for the polarization perpendicular to the wall plane.

To summarize, the component $\tilde{P}_1$ is very sensitive to wall orientation angle α with respect to the crystallographic plane. Also $\tilde{P}_1$ is typically an order of magnitude smaller than $\tilde{P}_2$, because it is suppressed by a depolarization field. Maximal values of the components $\tilde{P}_2$ and P_3 are typically of the same order since both are not affected by the depolarization field; but $\tilde{P}_2$ is a bit smaller than P_3 and rather sensitive to the angle α. Naturally, maximal value of P_3 coincides with $BaTiO_3$ spontaneous polarization value.

IV. ELECTRONIC PHENOMENA AT THE 180-DEGREE DOMAIN WALLS

The presence of Néel component $\tilde{P}_1$ leads to either accumulation or depletion of free carriers near the wall, potentially affecting the wall conductivity. Note that the DW conductivity mechanism stemming from the screening of the potential jump caused by depolarization field[4,46–48] has been justified by recent c-AFM studies of charged DWs in $LiNbO_3$,[49] nominally uncharged DWs in $BiFeO_3$,[8,50–53] and $Pb(Zr,Ti)O_3$.[54,55] DWs, vortex structures, and nanodomains in the ferroelectrics exhibit strongly enhanced c-AFM contrast in comparison with single-domain regions. In parallel, LGD theory was successfully used to evolve an analytical treatment of the carrier accumulation by both incline (and thus charged) and nominally uncharged domain walls in uniaxial ferroelectric $LiNbO_3$,[56] multiaxial ferroelectrics-ferroelastics $Pb(Zr,Ti)O_3$,[32] $BiFeO_3$,[57] and incipient ferroelectric-ferroelastic $CaTiO_3$.[58] Here we explore the electronic phenomena induced by the Néel component, and establish the potential for exploring symmetry breaking transitions at the walls by c-AFM.

A. Statement of the problem for the domain wall conductance

The conductivity enhancement in the domain wall is caused by the potential variation inside the wall. Here we assume that the concentration of holes is negligible and the conductivity is purely of n type.[43] The potential well/hump leads to higher/lower electron concentration in the DW due to the local band bending (see sketches in Fig. 7 for chiral and achiral walls).

TABLE I. Maximal value of polarization components calculated with and without flexoelectric coupling.

Maximal value of polarization component	Temperature							
	140 K, $\alpha = \pi/3$		180 K, $\alpha = \pi/3$		140 K, $\alpha = \pi/2$		180 K, $\alpha = \pi/2$	
	$F_{ij} = 0$	$F_{ij} \neq 0$	$F_{ij} = 0$	$F_{ij} \neq 0$	$F_{ij} = 0$	$F_{ij} \neq 0$	$F_{ij} = 0$	$F_{ij} \neq 0$
$\tilde{P}_1^{\max}(\mu C/cm^2)$	0	0.054	0	0.047	0.109	0.112	0.093	0.096
$\tilde{P}_2^{\max}(\mu C/cm^2)$	11.3	11.3	10.9	10.9	23.9	24.6	22.5	23.2
$\tilde{P}_3^{\max}(\mu C/cm^2)$	37.5	37.5	36.2	36.2	37.5	37.5	36.2	36.2

In the general case, analysis of electronic phenomena at the walls requires self-consistent solution of the GLD problem coupled to appropriate carrier statistics and Poisson-type equation describing potential redistribution due to the presence of electrons. Here we show numerically that for realistic charge carriers concentration in BTO the screening of the bound charge by electrons is negligible, and hence their distribution can be found with sufficient accuracy in the dielectric limit. In this approximation the potential φ is found from the expression

$$\varphi(\tilde{x}_1) \approx \frac{1}{\varepsilon_0 \varepsilon_b} \int_{-\infty}^{\tilde{x}_1} d\tilde{x} P_1(\tilde{x}). \tag{5}$$

The electron density $n(\tilde{x}_1)$ distribution is estimated as[59]

$$n(\tilde{x}_1) = \int_0^{\infty} d\varepsilon \, g_n(\varepsilon) f[\varepsilon + E_C - E_F - e\varphi(\tilde{x}_1)]$$
$$\approx n_c \exp\left[\frac{E_F - E_C + e\varphi(\tilde{x}_1)}{k_B T}\right], \tag{6}$$

where $g_n(\varepsilon) = \sqrt{2m_n^3 \varepsilon}/(\pi^2 \hbar^3)$ is the energy density of states in the effective mass approximation, m_n is the effective mass; $f(x) = [1 + \exp(x/k_B T)]^{-1}$ is the Fermi-Dirac distribution function, $k_B = 1.3807 \times 10^{-23}$ J/K, T is the absolute temperature, E_F is Fermi level position, E_C is the bottom of the conductive band, and $e = 1.6 \times 10^{-19}$ C is the electron charge. Approximate equality in Eq. (6) corresponds to the Boltzmann approximation for which the density of states in the conduction band $n_c = \sqrt{\pi m_n^3 k_B^3 T^3}/(\sqrt{2}\pi^2 \hbar^3)$. We checked that the Boltzmann approximation works adequately until $e|\varphi| \leqslant 5k_B T$. Fermi level position $E_F(T)$ in the frame of our approximation may be found in terms of electron concentration in the single-domain region $n_0(T) = n_c \exp[(E_F - E_C)/k_B T]$ as $E_F(T) = E_C + k_B T \ln(n_0/n_c)$.

Note that here we do not take into account deformation potential,[60,61] because we consider the model case of the nondegenerated simple band structure and use the effective mass approximation. For the case a shallow donor level and the conductive band edge are shifted as a whole with the strain.[62] We further postulate the continuity of the band structure across the DW. Rigorously speaking the potential barrier or well $\varphi(\tilde{x}_1)$ should be included into the quantum-mechanical treatment since quantization should exist in the direction transverse to the wall, which has thickness ~1 nm. Here we are interested in conductivity along the DW where no quantization occurs. We calculate the potential jump $\varphi(\tilde{x}_1)$ within continuum media theory and stipulate that results obtained for the carrier's accumulation/depletion across the DW are qualitatively valid and will be justified by a rigorous quantum-mechanical approach elsewhere. Results of the numerical modeling for the DW polarization vector structure, electric potential, and charge carriers redistribution across the domain wall are discussed below.

B. Phase transition detection in DW by c-AFM contrast

Since the $\tilde{P}_1$ profile is antisymmetric for achiral DW, the corresponding potential barrier $\varphi(\tilde{x}_1)$ is symmetric, while it can be asymmetric for achiral DWs. Symmetric barriers $\varphi(\tilde{x}_1)$ accumulate electrons with maximal density $n_{\max}$ [Fig. 7(a)]. Asymmetric double barriers can attract the electrons in some

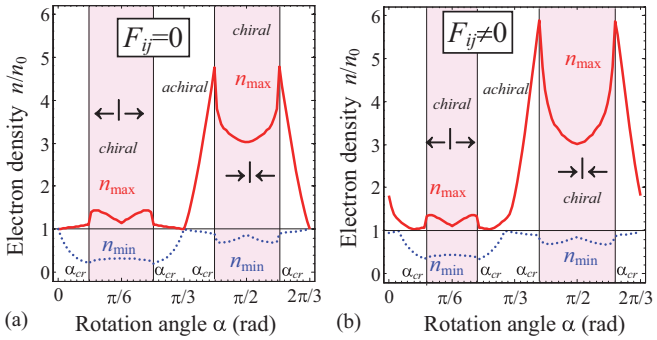

FIG. 8. (Color online) Relative maximal $n_{\max}/n_0$ and minimal $n_{\min}/n_0$ electron density vs the DW rotation angle α calculated in BTO at 180 K without flexoelectric coupling $F_{ij} = 0$ (a) and with flexoelectric coupling $F_{11} = 2.46$, $F_{12} = 0.48$, $F_{44} = 0.05$ in 10^{-11} m^3/C (b).

spatial regions with maximal density $n_{\max}$ and repulse them from the other regions with minimal density $n_{\min}$ [Fig. 7(b)]. The most intriguing situation can appear in the point of the wall chiral-achiral phase transition, i.e., at rotation angles around the critical ones α_{cr}. The chiral-achiral phase transition can be revealed by local c-AFM measurements of the cylindrical walls since c-AFM contrast is regarded proportional to the relative electron density $n(\tilde{x}_1)/n_0$.[54] Figure 8 illustrates the rotation anisotropy of the relative density $n(\tilde{x}_1)/n_0$. Exactly two sharp maxima on $n_{\max}$ and breaks $n_{\min}$ on Fig. 8 corresponds to the chiral-achiral phase transitions occurring at $\alpha_{cr}^m \approx \pi/6 \pm \pi/12 + m\pi/3$. Without flexoelectric coupling there is no c-AFM contrast for the angles $\alpha = m\pi/3$ corresponding to the absence of the component $\tilde{P}_1$ [see Figs. 8(a) and 2(d)]. Flexoelectric coupling leads to nonzero perpendicular component $\tilde{P}_1$ for all α and thus to nonzero contrast; also it slightly shifts the critical angles and create the symmetric potential structure well-barrier-well around rotation angle $\pi/3$ [see Figs. 8(b) and 6(a)]. Results shown in Fig. 8 for rhombohedral BTO look principally different from the ones presented in Ref. 59 for rhombohedral $BiFeO_3$. This difference may be explained because in $BiFeO_3$ the domain walls are only of achiral type, and the coupling between $\tilde{P}_1$ and $\tilde{P}_2$ components is not so strong.

Strong asymmetry in the electron density distributions in the α regions $\pi/6 \pm \pi/12$ and $\pi/2 \pm \pi/12$ originated from the fact that DWs have mainly tail-to-tail structure ($\leftarrow | \rightarrow$) with respect to $\tilde{P}_1$ at $\pi/6 \pm \pi/12$, and head-to-head structure ($\rightarrow | \leftarrow$) at $\pi/2 \pm \pi/12$.

The potential barrier (or well) $\varphi(\tilde{x}_1)$ and electron density $n(\tilde{x}_1)$ profiles calculated for different wall orientations are shown in Fig. 9. The walls oriented near α_{cr} corresponding to chiral-achiral phase transition have maximal electron accumulation, because polarization component $\tilde{P}_1$ is maximal there [see Fig. 6(a)]. One can see from Fig. 9(b) that maximal electron density $n(\tilde{x}_1)$ is about four times higher than the electron density n_0 in the single-domain region of BTO. This means that the wall relative conductivity at the wall becomes at least several times higher than in the single-domain region, i.e., the ratio $\sigma_{\max}/\sigma(\pm\infty) \gg 1$. Such contrast is pronounced and thus can be easily detected by c-AFM.

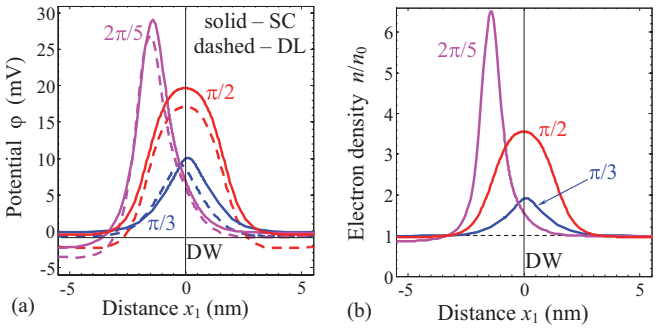

FIG. 9. (Color online) (a) Profiles of potential $\varphi(\tilde{x}_1)$ and (b) relative electron density $n(\tilde{x}_1)/n_0$ calculated across the DW for rotation angles $\alpha = \pi/3, 2\pi/5, \pi/2$ (specified near the curves), BTO at temperature 180 K, flexoelectric coefficients $F_{11} = 2.46$, $F_{12} = 0.48$, $F_{44} = 0.05$ in 10^{-11} m^3/C. Solid curves in plot (a) correspond to full-scale calculations with account of semiconducting properties: $n_0 = 3 \times 10^{22}$ m^{-3} (SC); dashed curves are calculated in dielectric limit $n_0 = 0$ (DL).

Temperature dependence of the c-AFM contrast of chiral walls, calculated as relative carrier density $n_{\max}(\tilde{x}_1)/n_0$ is shown in Fig. 10(a). In the Boltzmann approximation the contrast exponentially increases with the temperature decrease since $n \approx n_0(T)\exp(e\varphi/k_BT)$. At temperatures lower than 50 K the wall c-AFM contrast between the wall and the single-domain region becomes more than 10 times even for

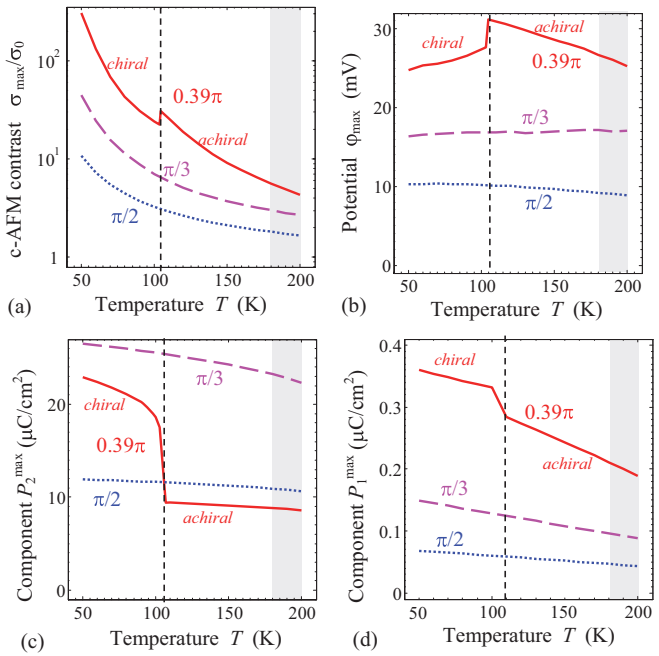

FIG. 10. (Color online) (a) Temperature dependence of the maximal c-AFM contrast $\sigma_{\max}/\sigma_0$; (b) potential jump $\varphi_{\max}$; and components (c) $\tilde{P}_2$ and (d) $\tilde{P}_1$ at DW in rhombohedral BTO calculated for different rotation angles $\alpha = \pi/2, \pi/3, 0.39\pi$ specified near the curves. Note that the angles $\alpha = \pi/3$ and $\alpha = \pi/2$ correspond to the DW with minimal and maximal energy, and one can see that even in the limiting cases the DWs are more conductive than the bulk. Gray rectangles indicate the region of orthorhombic and rhombohedral phases coexistence.

the case of the most weakly conducting walls corresponding to rotation angles $\alpha = \pi/3 + 2m\pi/3$. The angle $\alpha = \pi/3$ corresponds to the DW with minimal energy. For other rotation angles (e.g., for $\alpha = 0.39\pi, \pi/2$) the c-AFM contrast can be $50 - 500$ times higher than the single-domain one. The angle $\alpha = \pi/2$ corresponds to the DW with maximal energy. Note that the concentration n_0 strongly decreases with temperature decrease as shown in Fig. S4.[38]

Hence we suggest that the phase transition in the wall structure can be detected by the jump on the c-AFM contrast temperature dependence. Such a jump takes place for example at $T^*_{\rm cr} \approx 105$ K for the angle $\alpha^*_{\rm cr} = 0.39\pi$, which exactly corresponds to the abrupt phase transition in the wall structure, which is slightly shifted from the value $\alpha_{\rm cr} = 5\pi/12$ by the flexoelectric effect. Strong correlation between the c-AFM contrast [Fig. 10(a)], maximal potential at the wall $\varphi_{\max}(\tilde{x}_1)$ [Fig. 10(b)], amplitudes of $\tilde{P}_2$ [Fig. 10(c)], and $\tilde{P}_1$ [Fig. 10(d)] can be predicted from our study. Thus we hope that our calculations can stimulate further experimental c-AFM studies of the wall conduction in BTO, other ferroelectrics, and multiferroics in a wide temperature range since the studies can give insight to the wall polar structure and conductivity correlations, as well as quantitative information of the flexoelectric coupling strength.

V. SUMMARY

The structure, energetics, and electronic phenomena on the 180-degree domain wall in rhombohedral BTO are investigated as functions of wall orientation. It is shown that there are six energetically favorable wall orientations corresponding to $\{110\}$ planes, while $\{211\}$ orientations correspond to energy maxima. The minima are always degenerated, the flexoelectric effect can shift the degeneracy of the maxima, splitting them into two triplets. This is consistent with the presence of a mirror plane at $\{110\}$ and its absence at $\{211\}$. Another impact of the flexoelectric effect is that the polarization component perpendicular to the domain wall plane is nonzero for any wall orientation (0 for $\{110\}$ wall in its absence). Thus the flexoelectric effect reveals the true symmetry of the problem.

Domain walls are shown to be of mixed Ising-Bloch-Néel type for all orientations. Although the domain walls with $\{211\}$ and $\{110\}$ orientations are shown to have sufficiently different structures, achiral and chiral, the phase transition from achiral to chiral state can be achieved either by varying the wall orientation at fixed temperature or by temperature change at constant orientation. We further predict the existence of 1D defects similar to the cross-tie defects in the ferromagnetic Bloch domain walls as a consequence of such transition.

We further analyze electronic properties of such walls and suggest detecting the structural phase change inside the domain walls by c-AFM contrast due to the correlation of the domain wall structure and free charge accumulation, driven by the depolarizing field. Depending on the temperature and orientation, the conductivity of the wall may be one or even two orders of magnitude higher than in the single-domain region. Achiral-chiral phase transition in the wall is accompanied with rapid change of the wall c-AFM contrast. In this context c-AFM appears to be a promising tool for the detection of structural phase transitions inside domain walls.

ACKNOWLEDGMENTS

A.N.M. and E.A.E. gratefully acknowledge multiple discussions, useful suggestions, and critical remarks from Professor N. V. Morozovsky. E.A.E. and A.N.M. are thankful to NAS of Ukraine and State Fund of Fundamental Research of Ukraine (SFFR-NSF project UU48/002) for support. P.V.Y., A.K.T., and N.S. acknowledge the Swiss National Science foundation for financial support. The research of P.V.Y., A.K.T. and N.S., leading to these results, has received funding from the European Research Council under the EU 7th Framework Program (FP7/2007-2013) / ERC grant agreement n° [268058] S.V.K.'s research is supported by the US Department of Energy, Basic Energy Sciences, Materials Sciences and Engineering Division.

*Corresponding author: anna.n.morozovska@gmail.com

[1] W. Cao and C. Randall, Solid State Commun. **86**, 435 (1993).
[2] S. Stemmer, S. K. Streiffer, F. Ernst, and M. Rühle, Philos. Mag. A **71**, 713 (1995).
[3] V. A. Zhirnov, Zh. Eksp. Teor. Fiz. **35**, 1175 (1958) [Sov. Phys. JETP **35**, 822 (1959)].
[4] B. M. Darinskii and V. N. Fedosov, Sov. Phys. Solid State **13**, 17 (1971).
[5] W. Cao and L. E. Cross, Phys. Rev. B **44**, 5 (1991).
[6] P. Marton, I. Rychetsky, and J. Hlinka, Phys. Rev. B **81**, 144125 (2010).
[7] C.-L. Jia, S.-B. Mi, K. Urban, I. Vrejoiu, M. Alexe, and D. Hesse, Nat. Mater. **7**, 57 (2007).
[8] J. Seidel, L. W. Martin, Q. He, Q. Zhan, Y.-H. Chu, A. Rother, M. E. Hawkridge, P. Maksymovych, P. Yu, M. Gajek, N. Balke, S. V. Kalinin, S. Gemming, F. Wang, G. Catalan, J. F. Scott, N. A. Spaldin, J. Orenstein, and R. Ramesh, Nat. Mater. **8**, 229 (2009).
[9] A. Y. Borisevich, O. S. Ovchinnikov, H. J. Chang, M. P. Oxley, P. Yu, J. Seidel, E. A. Eliseev, A. N. Morozovska, R. Ramesh, S. J. Pennycook, and S. V. Kalinin, ACS Nano **4**, 6071 (2010).
[10] C.-L. Jia, K. W. Urban, M. Alexe, D. Hesse, and I. Vrejoiu, Science **331**, 1420 (2011).
[11] M. Daraktchiev, G. Catalan, and J. F. Scott, Phys. Rev. B **81**, 224118 (2010).
[12] D. A. Scrymgeour, V. Gopalan, A. Itagi, A. Saxena, and P. J. Swart, Phys. Rev. B **71**, 184110 (2005).
[13] M. Y. Gureev, A. K. Tagantsev, and N. Setter, Phys. Rev. B **83**, 184104 (2011).
[14] V. Stepkova, P. Marton, and J. Hlinka, J. Phys.: Condens. Matter **24**, 212201 (2012).
[15] I. A. Kornev, H. Fu, and L. Bellaiche. J. Mater. Sci. **41**, 137 (2006).
[16] B.-K. Lai, I. Ponomareva, I. A. Kornev, L. Bellaiche, and G. J. Salamo, Phys. Rev. B **75**, 085412 (2007).
[17] M. Taherinejad, D. Vanderbilt, P. Marton, V. Stepkova, and J. Hlinka, Phys. Rev. B **86**, 155138 (2012).
[18] A. P. Pyatakov and A. K. Zvezdin, Eur. Phys. J. B **71**, 419 (2009).
[19] B. Houchmandzadeh, J. Lajzerowicz, and E. K. H. Salje, J. Phys.: Condens. Matter **4**, 9779 (1992).
[20] M. Mostovoy, Phys. Rev. Lett. **96**, 067601 (2006).
[21] J. Lajzerowicz and J. J. Niez, J. Phys. Lett. **40**, 165 (1979).
[22] V. S. Mashkevich and K. B. Tolpygo, Zh. Eksp. Teor. Fiz. **31**, 520 (1957) [Sov. Phys. JETP **4**, 455 (1957)].
[23] A. K. Tagantsev, Phys. Rev B **34**, 5883 (1986).
[24] G. Catalan, L. J. Sinnamon, and J. M. Gregg, J. Phys.: Condens. Matter **16**, 2253 (2004).
[25] G. Catalan, B. Noheda, J. McAneney, L. J. Sinnamon, and J. M. Gregg, Phys. Rev. B **72**, 020102 (2005).
[26] R. Maranganti, N. D. Sharma, and P. Sharma, Phys. Rev. B **74**, 014110 (2006).
[27] M. S. Majdoub, P. Sharma, and T. Cagin, Phys. Rev. B **77**, 125424 (2008).
[28] M. S. Majdoub, R. Maranganti, and P. Sharma, Phys. Rev. B **79**, 115412 (2009).
[29] E. A. Eliseev, A. N. Morozovska, M. D. Glinchuk, and R. Blinc, Phys. Rev. B **79**, 165433 (2009).
[30] D. Lee, R. K. Behera, P. Wu, H. Xu, S. B. Sinnott, S. R. Phillpot, L. Q. Chen, and V. Gopalan, Phys. Rev. B **80**, 060102(R) (2009).
[31] R. K. Behera, C.-W. Lee, D. Lee, A. N. Morozovska, S. B. Sinnott, A. Asthagiri, V. Gopalan, and S. R. Phillpot, J. Phys.: Condens. Matter **23**, 175902 (2011).
[32] E. A. Eliseev, A. N. Morozovska, G. S. Svechnikov, P. Maksymovych, and S. V. Kalinin, Phys. Rev. B **85**, 045312 (2012).
[33] A. K. Tagantsev, E. Courtens, and L. Arzel, Phys. Rev. B **64**, 224107 (2001).
[34] J. Hlinka and P. Márton, Phys. Rev. B **74**, 104104 (2006).
[35] A. J. Bell, J. Appl. Phys. **89**, 3907 (2001).
[36] W. Ma and L. E. Cross, Appl. Phys. Lett. **88**, 232902 (2006).
[37] I. Ponomareva, A. K. Tagantsev, and L. Bellaiche, Phys. Rev. B **85**, 104101 (2012).
[38] See Supplemental Material at http://link.aps.org/supplemental/10.1103/PhysRevB.87.054111 for details.
[39] G. A. Korn and T. M. Korn, *Mathematical Handbook for Scientists and Engineers* (McGraw-Hill, New York, 1961).
[40] A. K. Tagantsev and G. Gerra, J. Appl. Phys. **100**, 051607 (2006).
[41] P. V. Yudin, A. K. Tagantsev, E. A. Eliseev, A. N. Morozovska, and N. Setter, Phys. Rev. B **86**, 134102 (2012).
[42] N. A. Pertsev, A. G. Zembilgotov, and A. K. Tagantsev, Phys. Rev. Lett. **80**, 1988 (1998).
[43] F. Jona and G. Shirane, *Ferroelectric Crystals* (Dover, New York, 1993).
[44] B. Houchmandzadeh, J. Lajzerowicz, and E. K. H. Salje, J. Phys. Condens. Matter **3**, 5163 (1991).
[45] N. D. Sharma, C. M. Landis, and P. Sharma, J. Appl. Phys. **108**, 024304 (2010).
[46] G. M. Guro, I. I. Ivanchik, and N. F. Kovtonyuk, Sov. Solid State Phys. **11**, 1956 (1969).
[47] B. M. Vul, G. M. Guro, and I. I. Ivanchik, Ferroelectrics **6**, 29 (1973).
[48] D. Meier, J. Seidel, A. Cano, K. Delaney, Y. Kumagai, M. Mostovoy, N. A. Spaldin, R. Ramesh, and M. Fiebig, Nat. Mater. **11**, 284 (2012).
[49] M. Schröder, A. Haußmann, A. Thiessen, E. Soergel, T. Woike, and L. M. Eng, Adv. Funct. Mater. **22**, 3936 (2012).
[50] J. Seidel, P. Maksymovych, Y. Batra, A. Katan, S.-Y. Yang, Q. He, A. P. Baddorf, S. V. Kalinin, C.-H. Yang, J.-C. Yang, Y.-H. Chu, E. K. H. Salje, H. Wormeester, M. Salmeron, and R. Ramesh, Phys. Rev. Lett. **105**, 197603 (2010).

[51] S. Farokhipoor and B. Noheda, Phys. Rev. Lett. **107**, 127601 (2011).
[52] R. K. Vasudevan, A. N. Morozovska, E. A. Eliseev, J. Britson, J.-C. Yang, Y.-H. Chu, P. Maksymovych, L. Q. Chen, V. Nagarajan, and S. V. Kalinin, Nano Lett. **12**, 5524 (2012).
[53] N. Balke, B. Winchester, W. Ren, Y. H. Chu, A. N. Morozovska, E. A. Eliseev, M. Huijben, R. K. Vasudevan, P. Maksymovych, J. Britson, S. Jesse, I. Kornev, R. Ramesh, L. Bellaiche, L. Q. Chen, and S. V. Kalinin, Nat. Phys. **8**, 81 (2012).
[54] J. Guyonnet, I. Gaponenko, S. Gariglio, and P. Paruch, Adv. Mater. **23**, 5377 (2011).
[55] P. Maksymovych, A. N. Morozovska, P. Yu, E. A. Eliseev, Y. H. Chu, R. Ramesh, A. P. Baddorf, and S. V. Kalinin, Nano Lett. **12**, 209 (2012).
[56] E. A. Eliseev, A. N. Morozovska, G. S. Svechnikov, V. Gopalan, and V. Ya. Shur, Phys. Rev. B **83**, 235313 (2011).
[57] A. N. Morozovska, R. K. Vasudevan, P. Maksymovych, S. V. Kalinin, and E. A. Eliseev, Phys. Rev. B **86**, 085315 (2012).
[58] E. A. Eliseev, A. N. Morozovska, Y. Gu, A. Y. Borisevich, L.-Q. Chen, V. Gopalan, and S. V. Kalinin, Phys. Rev. B **86**, 085416 (2012).
[59] A. I. Anselm, *Introduction to Semiconductor Theory* (Prentice-Hall, Englewood Cliffs, NJ, 1981), see p. 346, Eq. (2.18b).
[60] Y. Sun, S. E. Thompson, and T. Nishida, J. Appl. Phys. **101**, 104503 (2007).
[61] R. F. Berger, C. J. Fennie, and J. B. Neaton, Phys. Rev. Lett. **107**, 146804 (2011).
[62] G. L. Bir and G. E. Pikys, *Symmetry and Deformation Effects in Semiconductors* (Nauka, Moscow, 1972), Chap. 7.
[63] $BaTiO_3$ undergoes the rhombohedral-orthorhombic first order phase transition at 183 K under cooling, and the orthorhombic-rhombohedral transition at 203 K under heating. So the temperature range of width 20 K between 183 and 203 K is the temperature hysteresis range, where both these phases coexist, where the orthorhombic phase is stable and the rhombohedral is metastable for the chosen material parameters. The orthorhombic phase becomes unstable at temperatures lower than 183 K.
[64] Note that the values of the flexoelectric coefficients calculated for $BaTiO_3$ in the paper comes from *ab initio* theory. The values $F_{11} = 2.46$, $F_{12} = 0.48$, $F_{44} = 0.05$ in 10^{-11} m^3/C are essentially smaller than the ones $\sim$(5–10) $\times$ 10^{-10} m^3/C measured by Cross *et al*. for $PbZrTiO_3$, but are in agreement with microscopic theoretical estimations made by Kogan [Sov. Phys. Solid State **5**, 2069 (1964)]; ($f \sim 4$ V and so $F \sim 10^{-11}$ m^3/C), as well as with the values measured experimentally by Zubko *et al*. for $SrTiO_3$, $F_{11} = -1.38$, $F_{12} = 0.66$, $F_{44} = 0.848 \times 10^{-11}$ m^3/C. Independent recent microscopic calculations by Hong and Vanderbilt [Phys. Rev. B **84**, 180101(R) (2011)] speak in favor of the Kogan estimation validity.